Available online at website: https://journal.bcrec.id/index.php/bcrec

Bulletin of Chemical Reaction Engineering & Catalysis, 20 (4) 2025, 607-623

Original Research Article

# Driving Photocatalytic Efficiency through Controlled Cobalt–Iron and Cobalt–Nickel Ratios for Methylene Blue Degradation

**Maria Ulfa[1*], Istinganah Saetu Rohmah[1], Cindy Nur Anggreani[1]**

*Chemistry Education Study Program, Faculty of Teacher Training and Education, Sebelas Maret University, Jl. Ir. Sutami 36A, Surakarta 57126, Indonesia.*

*Received: 9th June 2025; Revised: 10th September 2025; Accepted: 11th September 2025*
*Available online: 18th September 2025; Published regularly: December 2025*

## Abstract

This study explores the development of nanostructured photocatalytic materials based on cobalt–iron ($CoFe_{1-2}$) and cobalt–nickel ($CoNi_{1-1}$) systems for the degradation of methylene blue, a persistent organic pollutant commonly found in textile wastewater. As the textile industry contributes significantly to environmental pollution through the discharge of recalcitrant dyes, this work aims to offer an effective and sustainable solution via visible-light-driven photocatalysis. The synthesis strategy employed a hard-template approach using mesoporous silica-gelatin composite (SPG-20), prepared from a mixture of P123 and gelatin under acidic conditions. Following hydrothermal treatment and calcination, the SPG-20 template was acid-activated to enhance surface reactivity. Metal precursors—$Co(NO_3)_2.6H_2O$ with either $Fe(NO_3)_3.9H_2O$ or $Ni(NO_3)_2.6H_2O$—were infiltrated into the template with citric acid as a chelating and carbon-forming agent. The composite underwent controlled thermal treatment to embed metal species into a confined carbon matrix, followed by alkaline etching to remove the silica scaffold and yield $CoFe_{1-2}$ and $CoNi_{1-1}$ carbon nanostructures. Comprehensive characterizations, including XRD, FTIR, BET, UV-DRS, and UV–VIS spectroscopy, revealed that the materials exhibited nanocrystalline domains with low crystallinity and high specific surface area, favorable for photocatalytic activity. BET analysis indicated a greater surface area in $CoFe_{1-2}$ (104.526 $m^2/g$) than in $CoNi_{1-1}$ (83.160 $m^2/g$), correlating with a higher number of available active sites. The band gap of $CoFe_{1-2}$ (1.180 eV) supports efficient visible-light absorption, which, coupled with its higher microporosity, enables superior methylene blue degradation (85% within 90 minutes) compared to $CoNi_{1-1}$ (75%). Control experiments in the absence of light showed minimal degradation, confirming that the reaction is photocatalytic in nature. Adsorption kinetics followed a pseudo-first-order model, with $CoFe_{1-2}$ also exhibiting a higher adsorption capacity (171.184 mg/g). These findings demonstrate the potential of template-assisted synthesis in producing tunable, high-performance photocatalysts for practical applications in sustainable textile wastewater treatment.



***Keywords***: Cobalt; Iron; Nickel; Photocatalysist; Methylene Blue

***How to Cite***: Ulfa, M., Rohmah, I.S., Anggreani, C.N. (2025). Driving Photocatalytic Efficiency through Controlled Cobalt–Iron and Cobalt–Nickel Ratios for Methylene Blue Degradation. *Bulletin of Chemical Reaction Engineering & Catalysis*, 20 (4), 607-623. (doi: 10.9767/bcrec.20410)

***Permalink/DOI***: https://doi.org/10.9767/bcrec.20410

## 1. Introduction

The textile sector is recognized as a significant contributor to the generation of hazardous liquid wastes, especially the disposal of dye wastes such as methylene blue (MB) [1-3], which is toxic and resistant to natural degradation [4-7]. Utilization of photocatalyst-based methodologies for waste management presents a promising avenue, as it effectively degrades organic pollutants into environmentally friendly by-products [8-10]. However, the efficacy of photocatalysis is significantly influenced by the type and specific properties of the photocatalytic materials used [11,12].

* Corresponding Author.
Email: mariaulfa@staff.uns.ac.id (M. Ulfa)

Transition metal-based materials, including cobalt, iron, and nickel, have garnered extensive research interest as potential photocatalysts due to their favorable physical and chemical attributes that facilitate the formation of electron-hole pairs and the production of reactive species conducive to MB degradation [13-16]. For example, cobalt ferrite ($CoFe_2O_4$) and cobalt-nickel oxide ($CoNiO_2$) nanoparticles have shown significant effectiveness in enhancing the degradation rate of MB upon visible light irradiation [17-21]. The synergistic effect of these metals is known to tune the bandgap energy, broaden the light absorption, and reduce the electron-hole recombination rate, thereby enhancing the photocatalytic performance [22,23].

Previous investigations have shown that cobalt doping in $Fe_3O_4$ can reduce the band gap energy from 2.76 eV to 1.61 eV (directly) and enhance the photocatalytic activity toward MB, achieving optimal efficacy at 1% cobalt doping level [24]. Simultaneously, composites based on CO/Ni-MOF combined with BiOI have shown significant enhancement in light absorption and photocatalytic efficiency [25]. Furthermore, modifications in surface and pore architecture, as exemplified by $CoZn\text{-}Fe_2O_4/SiO_2$, have been shown to increase the specific surface area and pore size distribution, thereby accelerating the degradation process of MB [26].

However, there is still a significant lack of research that needs to be addressed. Most of the existing studies have only concentrated on isolated metal types or simple combinations, failing to systematically investigate the impact of various cobalt-iron and cobalt-nickel ratios on critical parameters such as surface area, pore size distribution, electron-hole recombination rate, crystallite dimensions, degree of crystallinity, and band gap energy. In fact, these factors are crucial in determining the photocatalytic efficiency and stability of materials in practical applications [27,28].

In addition, the synthetic approaches used in previous studies tend to be predominantly conventional, lacking the innovations necessary to precisely control the morphology, crystallite size, and metal distribution. These limitations result in substantial variability in yield and limit the optimization of photocatalyst performance for MB degradation. The originality of this study lies in the formulation of a novel synthetic technique that allows systematic regulation of the cobalt–iron and cobalt–nickel ratios, along with a comprehensive characterization of how these ratios affect the fundamental attributes of photocatalytic materials. The investigation focuses on elucidating the correlation between metal ratios and photocatalytic efficacy, surface area, pore size distribution, electron–hole recombination rate, crystallite dimensions, degree of crystallinity, and band gap energy, which have not been thoroughly examined in the context of Co–Fe and Co–Ni systems for MB degradation applications.

Furthermore, the study assesses the performance of the materials under conditions that closely resemble those encountered in textile industrial effluents, thereby ensuring that the findings are more applicable and relevant to the industrial context. Consequently, this study not only advances the fundamental science of photocatalytic materials but also offers a practical solution for environmentally sustainable textile wastewater treatment.

The primary goal of this research is to drive photocatalytic efficiency through controlling the ratios of cobalt-iron and cobalt-nickel in photocatalytic materials and to demonstrate the relationship between logarithmic ratios and material properties such as surface area, particle size distribution, and recombination. With this approach, it is hoped that optimal material compositions for photocatalytic applications in the textile industry would be discovered, as well as new knowledge about the fundamental mechanisms that optimize photocatalytic efficiency in cobalt-iron and cobalt-nickel systems [29].

## 2. Materials and Methods

### 2.1 Materials

All reagents were of analytical grade and used without further purification. Hydrochloric acid (HCl, 37%, molar mass 36.46 g/mol), ethanol ($C_2H_5OH$, 99.8%, molar mass 46.07 g/mol), citric acid monohydrate ($C_6H_8O_7.H_2O$, 99.5%, molar mass 192.12 g/mol), sodium hydroxide (NaOH, 2 M, molar mass 39.997 g/mol), and methylene blue (MB, dye content $\geqslant$ 82%, molar mass 319.85 g/mol) were purchased from Sigma-Aldrich, Merck KGaA. Transition metal precursors included nickel(II) carbonate hexahydrate ($NiCO_3.6H_2O$, $\geqslant$ 99%, molar mass 322.79 g/mol), cobalt(II) carbonate hexahydrate ($CoCO_3.6H_2O$, $\geqslant$ 98%, molar mass 323.03 g/mol), and iron(II) nitrate nonahydrate ($Fe(NO_3)_2.9H_2O$, $\geqslant$ 98%, molar mass 319.94 g/mol), all supplied by Sigma-Aldrich, Merck KGaA. Gelatin (Type B, average molar mass ~90,000 g/mol) was obtained from Gelita AG and used as a biopolymer template and nitrogen-rich carbon precursor. Deionized water (resistivity $\geqslant$ 18.2 MΩ.cm) from a Milli-Q system was used in all solution preparations.

### 2.2. Synthesis of Catalysts

The synthesis began with the preparation of a mesoporous silica-gelatin template (SPG-20), which served as a hard scaffold for structuring the carbon nanocomposite. A mixture of the nonionic

surfactant P123 and gelatin was prepared at a molar ratio of approximately 1:0.2, stirred at 40 °C for 3 hours under continuous agitation. During this process, a dilute hydrochloric acid solution (pH ≈ 2) was added dropwise to facilitate co-assembly. Tetraethyl orthosilicate (TEOS) was then added at a TEOS:P123 molar ratio of approximately 1:0.017, and the mixture was further stirred for 24 hours. The resulting gel was subjected to hydrothermal treatment at 90 °C for 24 hours, followed by vacuum filtration, washing with deionized water, and sequential drying at 70 °C and 100 °C. The dried material was calcined at 550 °C for 5 hours in static air to remove organic components, forming the SPG-20 silica-gelatin hard template. To enhance the surface reactivity, the template was soaked in 0.1 M HCl for 24 hours, then filtered, rinsed, and dried at 100 °C.

For metal infiltration, cobalt(II) nitrate and iron(III) nitrate were dissolved separately in deionized water and mixed to yield a Co:Fe molar ratio of approximately 1:4.16, based on a corresponding mass ratio of 1.8344:7.6385. The combined metal solution was stirred for 1 hour and subsequently impregnated into the acid-activated SPG-20 template. Citric acid monohydrate was added dropwise in a metal ion to citric acid molar ratio of approximately 1:1.2, serving as a chelating and carbon-forming agent. The suspension was stirred at 70 °C to evaporate water, then dried at 100 °C for 24 hours. This was followed by a pre-carbonization step at 250 °C for 5 hours to form a composite in which the metal ions were embedded in a carbonaceous matrix confined within the silica pores. To remove the template, the resulting composite was immersed in 1 M NaOH at 90 °C and stirred for 10 hours to selectively etch the silica phase. The solid was filtered, washed with deionized water to neutral pH, and dried at 60 °C overnight, yielding the final Co–Fe nanostructured carbon material.

A bimetallic Co–Ni variant was synthesized following the same procedure, using cobalt(II) nitrate and nickel(II) nitrate precursors in a Co:Ni molar ratio of approximately 1:1, derived from the reported mass ratio of 2.7406:2.7498. This parallel synthesis enabled comparative evaluation of cobalt-based binary systems with iron and nickel in influencing carbon microstructure and potential catalytic functionalities.

### 2.3. Photodegradation of Methylene Blue

The photocatalytic degradation of methylene blue (MB) was performed using a 0.2 L MB solution at a concentration of $2.0 \times 10^{-5}$ kg/L. A total of $5.0 \times 10^{-5}$ kg of photocatalyst was added to the solution in an Erlenmeyer flask, followed by a 30-minute dark adsorption phase to reach adsorption–desorption equilibrium. The suspension was then distributed into twelve dark glass vials, each containing 0.01 L of solution, under dark conditions inside the photocatalytic reactor. One vial was labeled as $C_0$ (0 min, representing the initial concentration before light irradiation). The remaining vials were placed on a shaker within the reactor without caps. Photocatalytic degradation commenced after 20 minutes by activating the visible light source and the shaker. Vials were withdrawn every 5 minutes up to 20 minutes, and then every 10 minutes until the 90th minute. After collection, each vial was sealed and stored in a completely dark container to prevent continued reaction. The absorbance of each sample was immediately measured using a UV-Vis spectrophotometer (Shimadzu UV-3600) at the maximum wavelength of 660 nm, corresponding to the absorption peak of methylene blue.

### 2.5. Characterizations

The instruments used for characterizing the samples in this study include X-Ray Diffraction (XRD) from Panalytical (Model PW3050/60), operated within a 2θ range of 5° to 80°, to determine the crystallinity and phase composition of the synthesized materials. The surface area and porosity were measured using the Brunauer-Emmett-Teller (BET) method with a Quantachrome Nova 1200e instrument. Fourier Transform Infrared Spectroscopy (FTIR), performed using a Shimadzu 21 spectrometer with a resolution of 0.5 $cm^{-1}$, was employed to analyze functional groups in the materials in the wavenumber range of 300–4000 $cm^{-1}$. Scanning Electron Microscopy with Energy Dispersive X-Ray (SEM-EDX) analysis was conducted using a JEOL JSM-700 microscope at a voltage of 15 kV to observe the surface morphology and elemental composition of the samples.

## 3. Results and Discussion

### 3.1. XRD Characterization

According to the X-ray diffraction data presented in the Table 1, Figure 1, both examined samples exhibit relatively small crystalline dimensions on the nanometer scale, accompanied by a low degree of crystallinity, which is characteristic of nanocrystalline materials that remain at the early stage of crystal formation. The $CoFe_{1-2}$ sample exhibits a crystalline dimension of 4.5219 nm, while the $CoNi_{1-1}$ sample presents a slightly larger crystalline dimension of 5.3423 nm. This variance in crystalline size indicates a significant impact of the transition metal composition on crystal growth during the synthesis process. In accordance with the research, the crystalline size in ferrite materials can be derived using the Scherrer equation, which takes into account the peak width at half

maximum (FWHM) in addition to the angular position of the diffraction [30]. The small crystalline size indicates that both samples belong to the realm of nanomaterials, where crystalline dimensions below 100 nm tend to exhibit different properties that are different from the bulk material [31].

Comparison of the crystalline sizes between the two samples shows that nickel substitution in the ferrite structure tends to produce slightly larger crystalline when compared to the pure cobalt ferrite framework. This phenomenon may originate from the difference in ionic radii between $Fe^{3+}$ and $Ni^{2+}$ ions, which affect the lattice parameters and crystal growth. Previous investigations have shown that the particle dimensions of ferrite can be modulated by a series of synthesis parameters, including temperature, precursor concentration, and synthesis methodology used [32].

The crystallinity degrees for both samples were observed to be very low, with $CoFe_{1-2}$ showing a crystallinity degree of 5.2327% and $CoNi_{1-1}$ revealing a crystallinity degree of 4.942%. Such low crystallinity values imply that most of the material structure remains in the amorphous phase, with only a small fraction achieving substantial crystallization. The reduced crystallinity degrees observed in both samples could be due to several factors, including suboptimal synthesis conditions, inadequate calcination temperatures, or insufficient heating duration for the formation of ideal crystal structures [33][34]. Research conducted on cobalt ferrite nanoparticles has shown that increasing the synthesis temperature can increase the degree of crystallinity of the material, as evidenced by samples synthesized at 60 °C, 80 °C, and 120 °C [35]. Samples produced at high temperatures exhibit sharper peak intensities and better crystallinity [36,37].

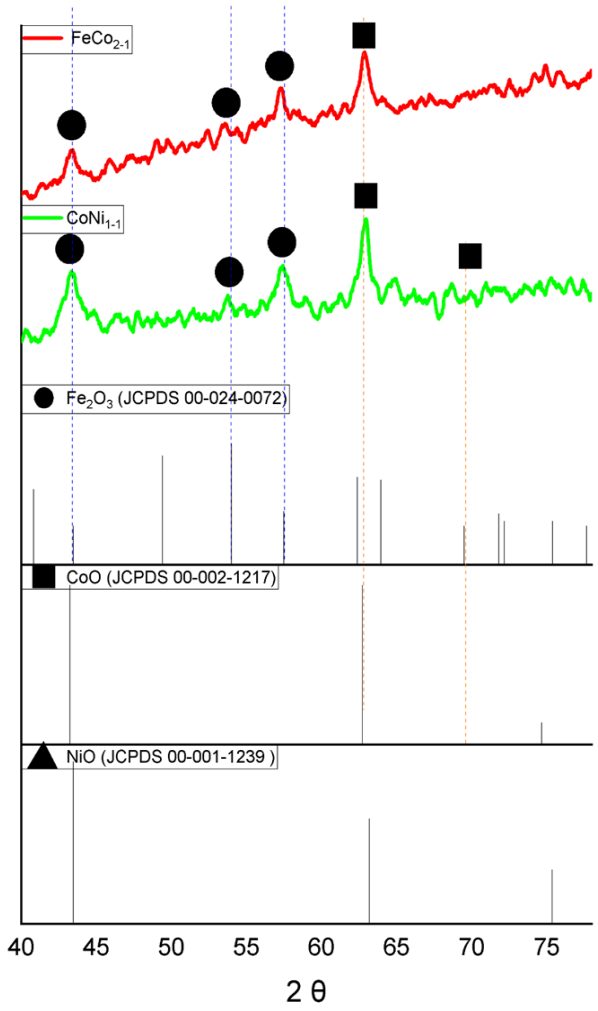


Figure 1. XRD Patterns of CoFe1-2 and CoNi1-1.

The interplay between small crystallinity dimensions and low crystallinity levels yields significant insights into the structural characteristics and properties of the resulting materials. Materials characterized by crystallinity sizes in the range of 4-5 nm are classified as ultra-small nanoparticles, which can exhibit superparamagnetic properties, especially in ferrite systems such as cobalt ferrite. Previous investigations have established that cobalt ferrite with crystallinity dimensions of approximately 13.25 nm continues to exhibit favorable magnetic properties, as evidenced by substantial magnetic saturation values [30].

The low degree of crystallinity observed in both specimens indicates that the materials mainly exhibit an amorphous phase. This characteristic can affect the magnetic, electrical, and catalytic behavior of the material, since the imperfect crystal framework reduces the regularity of the atomic arrangement and can lead to structural imperfections that impact the inherent properties of the substance. For certain applications, such as magnetic hyperthermia, materials with high crystallinity are usually required to achieve optimal magnetic response.

The small dimensions of the crystallites are generally associated with a large specific surface area. This large surface area is very beneficial in photocatalytic applications, as it offers more active sites for the adsorption of methylene blue molecules and promotes photochemical reactions. As research, the reduction in the particle size of the photocatalyst is correlated with the increase

Table 1. Crystallite size of $CoFe_{1-2}$ and $CoNi_{1-1}$ by XRD.

| Sample | *D* (nm) | Crystallinity (%) |
|---|---|---|
| $CoFe_{1-2}$ | 4.5219 | 5.2327 |
| $CoNi_{1-1}$ | 5.3423 | 4.942 |

in the surface area, thus facilitating greater direct interaction between the pollutant molecules and the catalyst surface. This process accelerates the charge transfer and improves the degradation efficiency [38].

In addition, the nanocrystalline architecture can effectively minimize the diffusion distance for charge carriers (electrons and holes), thereby reducing the possibility of recombination of electron-hole pairs before engaging with the target molecules. Wang *et al.* explained that nanoparticles on the nanometer scale can enhance charge separation and prolong the lifetime of electron-hole pairs, which are very important for the formation of reactive radicals (-OH and -$O_2$) during the photocatalytic process [39].

However, low crystallinity is not without its drawbacks. Materials that exhibit low crystallinity tend to have many structural defects (defect sites) such as vacancies, interstitials, and grain boundaries. These defects can serve several functions: they can act as charge trapping centers that facilitate the separation of electrons and holes, thereby improving photocatalytic performance. Conversely, excessive defects can cause recombination, which then reduces the efficacy of the photocatalyst. A study showed that the moderate presence of structural defects in semiconductor materials can enhance photocatalytic activity, but excess can impair performance due to increased charge recombination [40,41].

In the case of $CoFe_{1-2}$ and $CoNi_{1-1}$, low crystallinity likely contributes positively to photocatalytic activity by increasing the number of active and defect sites that can function as charge traps. However, to achieve optimal degradation efficiency for methylene blue, it is generally important to strike a balance between small crystallite size and high enough crystallinity to suppress charge recombination without introducing excessive detrimental defects. In addition, the transition metal composition in the material also plays an important role. The incorporation of Ni into the CoFe structure can change the band gap and enhance charge separation, thereby enhancing the photocatalytic activity depending on its composition and crystal configuration [42].

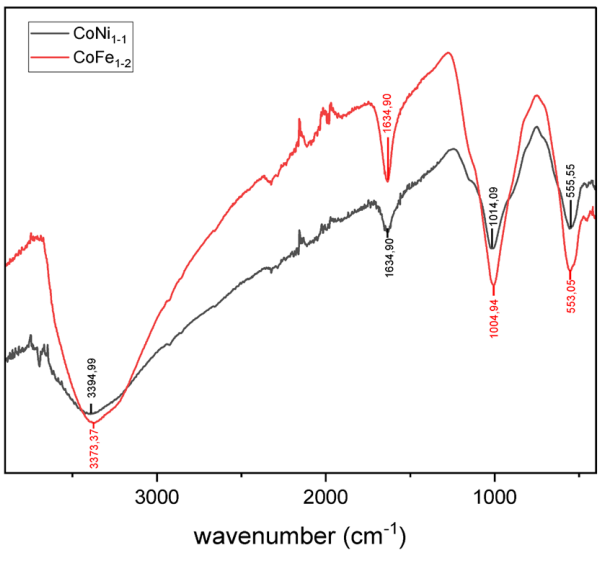


Figure 2. FTIR Spectra of $CoFe_{1-2}$ and $CoNi_{1-1}$.

### 3.2. FTIR Characterization

Based on the FTIR spectra illustrated in Figure 2, a comparative analysis is presented between two specimens, designated $CoNi_{1-1}$ (represented by the black line) and $CoFe_{1-2}$ (denoted by the red line), in the wavelength range of 4000-500 $cm^{-1}$. In the higher wavenumber region, around 3000-3500 $cm^{-1}$, both samples show broad and relatively weak absorption bands. Interpretation of the FTIR spectra shows that the absorption bands located in the range of 3650—3250 $cm^{-1}$ indicate hydrogen bonds as well as confirmation of oxygen-related bonds [43]. The presence of such bands is likely due to water molecules adsorbed on the surface of the ferrite nanoparticles or residual moisture present in the samples. In the fingerprint region spanning 1000-1500 $cm^{-1}$, the spectra reveal several complex peaks. This region is very important for the characterization of ferrite materials, as it includes specific information regarding the vibrational modes of the metal-oxygen bonds inherent in the spinel structure [44,45]. The peaks detected in this domain can shed light on the details of the cation distribution and the degree of inversion present in the ferrite crystal structure.

Of particular note in this analysis is the lower wavenumber segment below 1000 $cm^{-1}$, especially around 500-700 $cm^{-1}$. Generally, in ferrite spectra, two primary bands are observed in the range of 1000-300 $cm^{-1}$. The band associated with the higher frequencies is usually found in the range of 600-550 $cm^{-1}$, attributed to the tensile vibrations of the tetrahedral metal-oxygen bond, while the band associated with the lower frequencies is usually located below 450 $cm^{-1}$ and corresponds to the vibrational modes of the octahedral metal-oxygen bond [46].

The presented spectrum reveals characteristic peaks around 573 $cm^{-1}$ and 455 $cm^{-1}$, in good agreement with the literature related to cobalt ferrite materials [46]. The peak at high frequency (around 573 $cm^{-1}$) confirms the presence of Fe-O bonds located within the tetrahedral sites, while the peak at reduced frequency (around 455 $cm^{-1}$) indicates the presence of metal-oxygen bonds within the octahedral sites of the spinel structure.

The difference in intensity and variation of peak positions between the $CoNi_{1-1}$ and $CoFe_{1-2}$

samples indicates the difference in composition and distribution of cations in the crystal structure. The $CoFe_{1-2}$ sample shows a higher absorption intensity in certain regions, which can be ascribed to the variation in metal ion concentration and its corresponding influence on the bond vibrations in the spinel framework. In addition, the detection of a transition metal peak at around 420 $cm^{-1}$ further corroborates the presence of transition metal ions in the ferrite structure [46]. This analysis is consistent with the formation of a ferrite phase characterized by a spinel structure, in which metal ions are spatially distributed across various tetrahedral and octahedral sites.

### 3.3. BET Characterization

The investigation (Table 2, Figure 3) revealed that the $CoFe_{1-2}$ specimen exhibited a BET surface area of 104.526 $m^2/g$, surpassing the $CoNi_{1-1}$ sample, which recorded a value of 83.160 $m^2/g$. This difference is in line with previous studies showing that the synthesis method and chemical composition significantly affect the porosity characteristics of ferrite materials [47]. Further examination of the pore size distribution revealed a noteworthy feature, as both samples exhibited a surface area of mesoporous value of zero, indicating that the material is predominantly microporous. This is corroborated by the identical surface area of mesoporous and BET surface area values for both specimens, indicating that the total surface area is exclusively due to the contribution from micropores. This observation is consistent with findings from previous investigations that cobalt ferrite synthesized via the coprecipitation method tends to develop a structure with a predominance of micropores [46].

The total pore volume shows a significant contrast between the two samples, with $CoNi_{1-1}$ (0.2254 $cm^3/g$) exhibiting a larger pore volume than $CoFe_{1-2}$ (0.1875 $cm^3/g$). Although $CoNi_{1-1}$ has a reduced surface area, this larger pore volume indicates the presence of larger pores, as evidenced by the mean pore diameter, which is 9.96741 nm compared to 3.60646 nm for $CoFe_{1-2}$.

From a crystallographic perspective, these variations in porosity characteristics can be ascribed to the substitution effects of cations in the ferrite spinel framework. The study shows that $Ni^{2+}$ ions display different preferences in occupying octahedral and tetrahedral sites when compared to $Fe^{3+}$ ions, which could potentially affect the development and stability of the pore structure during the synthesis process [47]. The differences in ionic dimensions and crystal energies between nickel and iron result in variations in lattice parameters and micro-stresses, which ultimately modulate the morphological and textural features of the materials.

The dominant microporous architecture in both samples indicates the synthesis of nanoparticles characterized by substantial aggregation, resulting in narrowed interparticle spacing. This observation is in line with the XRD characterization results showing crystallite

Table 2. Porosity analysis of $CoFe_{1-2}$ and $CoNi_{1-1}$. $S_{BET}$: specific surface area calculated by BET method from $N_2$ adsorption; $S_{BJH}$: surface area from BJH desorption; $S_{mi}$: micropore surface area; $S_{me}$: mesopore surface area; $V_{tot}$: total pore volume; $d_P$: pore diameter obtained from BJH desorption branch.

| Sample | $S_{BET}$ ($m^2/g$) | $S_{BJH}$ ($m^2/g$) | $S_{mi}$($m^2/g$) | $S_{me}$($m^2/g$) | $V_{tot}$ (cc/g) | $D_P$(nm) |
|---|---|---|---|---|---|---|
| $CoFe_{1-2}$ | 104.526 | 90.4514 | 104.526 | 0 | 0.1875 | 3.60646 |
| $CoNi_{1-1}$ | 83.160 | 86.6101 | 83.160 | 0 | 0.2254 | 9.96741 |

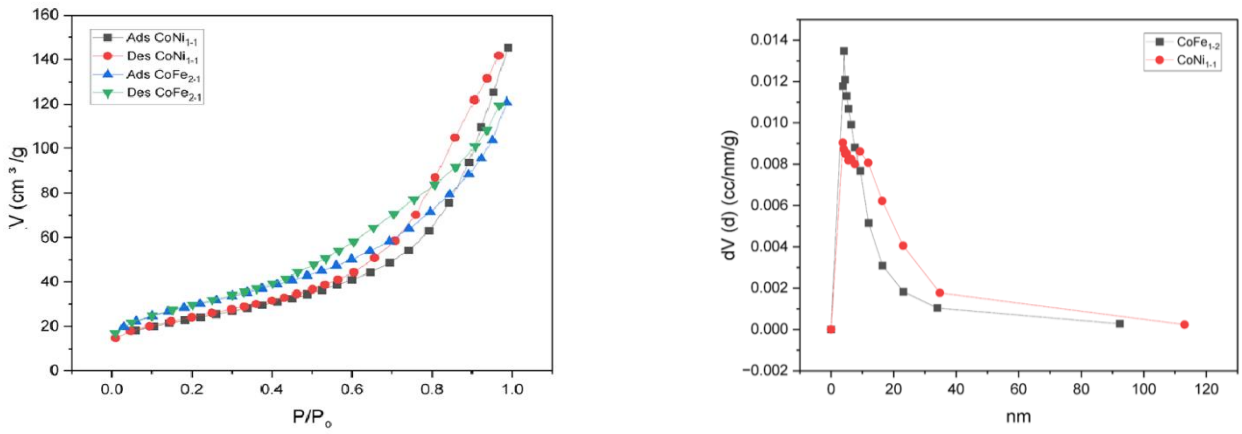


Figure 3. Isotherm Adsorption desorption and pore size distribution of $CoFe_{1-2}$ and $CoNi_{1-1}$.

dimensions in the nanometer range for ferrite materials produced via analogous methodologies. The contrasting pore size distributions between the two samples further indicate varying degrees of agglomeration, where $CoNi_{1-1}$ exhibit a more relaxed agglomeration, culminating in larger pores.

In terms of photocatalytic applications for methylene blue degradation, these different textural characteristics have significant consequences for catalytic efficacy. The increased specific surface area of $CoFe_{1-2}$ (104.526 $m^2/g$) offers an increased number of active sites for methylene blue molecule adsorption and photocatalytic reaction, theoretically enhancing degradation efficiency. Previous studies have established a positive correlation between BET surface area and photocatalytic activity in the context of organic dye degradation.

However, the reduced pore diameter of $CoFe_{1-2}$ (3.60646 nm) may impose diffusion limitations on methylene blue molecules, which have molecular dimensions of approximately 1.43 × 0.61 × 0.16 nm. In contrast, $coni^1$ with a larger pore diameter (9.96741 nm) may facilitate increased access of substrate molecules to the internal active sites, albeit at the expense of a reduced total surface area.

The observed increase in total pore volume in $CoNi_{1-1}$ indicates the potential enhancement of adsorption capacity, which is a critical early stage in the photocatalytic mechanism. The balance between adsorption and desorption of reaction products is crucial to maintain prolonged catalytic performance. The relatively more accessible pore architecture in $CoNi_{1-1}$ can promote the enhancement of mass transfer, thereby reducing the internal diffusion resistance that often acts as a limiting factor in heterogeneous photocatalytic frameworks.

From the perspective of electronic properties, the incorporation of $Ni^{2+}$ into the ferrite lattice can change the electronic band structure and optical characteristics of the material, directly affecting the light absorption and generation of electron-hole pairs. The integration of distinctive texture features with the changes in electronic properties can produce synergistic effects that are beneficial for the photocatalytic degradation of methylene blue.

Examination of the isotherm curves reveals that both samples conform to the Type IV isotherm classification according to the IUPAC standard [48]. The defining property of the Type IV isotherm is the manifestation of a hysteresis loop bridging the adsorption and desorption curves, which is clearly observed in both samples in the relatively high pressure range ($P/P^3 > 0.6$). The literature shows that Type IV isotherms appear when capillary condensation occurs, where gas condenses in the small capillary pores of a solid at pressures below the gas saturation pressure [49].

In the region of relatively low pressure ($P/P^3 < 0.4$), both samples show gradual nitrogen adsorption, indicating monolayer formation and initiation of multilayer development on the material surface. The initial segment of this Type IV isotherm is parallel to the corresponding Type II isotherm, indicating monolayer-multilayer adsorption since it follows the trajectory of the analogous portion of the Type II isotherm obtained from adsorptive interactions on the same surface area of a non-porous adsorbent [48].

A significant escalation in the adsorption volume is observed at $P/P^3$ approximately between 0.6–0.8, indicating the onset of capillary condensation within the mesopores of the material. This behavior is in line with the characteristics of mesoporous substances that have pore diameters ranging from 2 to 50 nm. The established hysteresis loops indicate the presence of pores with complex geometric configurations, where the pore filling and emptying processes occur at different pressures due to the effects of meniscus curvature and varying molecular interactions during adsorption and desorption [49].

Considering the morphology of the curves and the identified hysteresis loops, this isotherm can be categorized as a Type IV isotherm displaying hysteresis loops that likely belong to the H3 subclass according to the IUPAC categorization [50]. The H3 hysteresis loop is characterized by a steeper desorption branch relative to the adsorption branch and is usually associated with non-rigid particle aggregates forming slit-shaped pores [51,52].

A visible contrast between the $CoNi_{1-1}$ and $CoFe_{1-2}$ samples is evident in terms of the maximum adsorption capacity and the configuration of the hysteresis loops. The $CoFe_{1-2}$ sample shows a slightly increased adsorption capacity at saturation pressure, reaching approximately 120 $cm^3/g$, while the $CoNi_{1-1}$ reaches approximately 150 $cm^3/g$. These differences indicate the differences in total pore volume and pore size distribution between the two samples, which can be ascribed to the effects of different cation substitutions in the ferrite structure.

The $CoFe_{1-2}$ material exhibits a pore size distribution mainly characterized by mesopores, with a significant peak in the range of 2-5 nm, and the $dV/dD$ value reaches about 0.014 $cm^3/nm/g$. This distribution pattern indicates a material with a well-defined mesoporous structure, where the differential pore volume decreases exponentially with increasing pore dimensions. According to the IUPAC classification, this pore size range is categorized as mesoporous (2-50 nm),

which is very significant for the adsorption of medium-sized organic molecules such as methylene blue [53]. This property implies that the $CoFe_{1-2}$ material has a pore architecture that is adept at accommodating target molecules in the photocatalytic process.

The $CoNi_{1-1}$ material exhibits a comparable pore size distribution profile, albeit with reduced intensity, where the maximum *dV/dD* peak only reaches about 0.009 $cm^3.g^{-1}.nm^{-1}$ within the same pore size range. Although this distribution pattern is similar in shape to that of CoFe1-2, the lower differential pore volume suggests a reduction in pore accessibility and total pore volume, which may consequently influence the specific surface area. The difference in intensity is likely related to variations in the synthesis route or the intrinsic chemical composition that governs pore development.

Given that $CoFe_{1-2}$ exhibits a higher maximum differential pore volume, it is anticipated to exhibit superior photocatalytic efficacy compared to $CoNi_{1-1}$ in methylene blue degradation. The enlarged pore volume facilitates a larger adsorption capacity, which is a critical initial phase in heterogeneous photocatalysis. Effective adsorption increases the local concentration of pollutant molecules around the photocatalytic active sites, thereby increasing the possibility of oxidation reactions. Furthermore, the more developed pore structure in $CoFe_{1-2}$ enhances light penetration into the bulk material, which is essential for achieving optimal photocatalytic activation.

### 3.4. UV-DRS Characterization

The band gap energy value (Figure 4) of 1.180 eV, derived from UV-VIS DRS characterization, shows excellent agreement with the fundamental research conducted by Holinsworth *et al.*, who described the indirect band gap of $CoFe_2O_4$ at 1.17 ± 0.08 eV by optical absorption spectroscopy technique [54]. The agreement of these values confirms the accuracy of the characterization methodology used and the legitimacy of the electronic architecture of the synthesized compound. The band gap energy in this range indicates that the $CoFe_2O_4$ material is classified as a narrow band gap semiconductor, which exhibits enhanced light absorption capability in the visible spectrum compared to traditional semiconductors such as $TiO_2$, which has a band gap of about 3.2 eV.

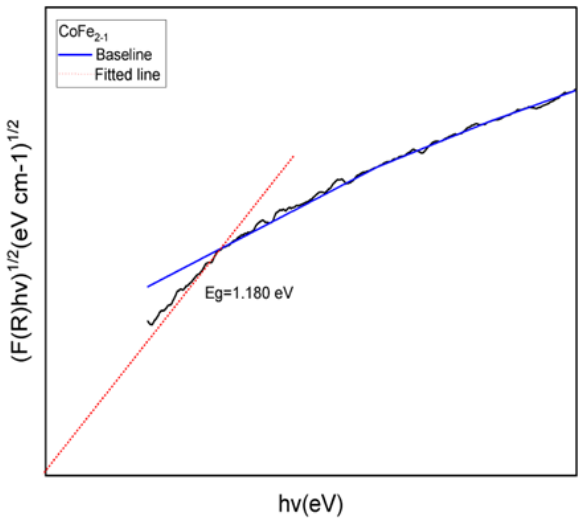


Figure 4. Band gap by Tauc plot of $CoFe_{1-2}$ sample.

This narrow band gap characteristic is very beneficial for photocatalytic applications, as it facilitates the exploitation of a broader light spectrum, covering visible light and, to some extent, near infrared radiation. According to semiconductor theory, the photon energy required for the excitation of electrons from the valence band to the conduction band should be equal to or exceed the band gap energy of the material [55]. With a measured value of 1.180 eV, the material can be activated by photons with wavelengths reaching around 1050 nm, thus covering most of the visible light spectrum and part of the near-infrared. This provides a noteworthy competitive advantage in practical photocatalytic applications, especially in utilizing sunlight as a viable energy source.

The band gap energy of 1.180 eV brings favorable implications for the photocatalytic efficacy in methylene blue degradation, especially regarding the efficiency of light absorption and the formation of electron-hole pairs. Methylene blue, characterized by its complex molecular architecture and extensive conjugated bonds, requires sufficient energy for effective photocatalytic oxidation. The relatively low band gap value allows the $CoFe_2O_4$ material to absorb photons with lower energy, thus utilizing the enhanced light intensity present in the solar spectrum to generate electron-hole pairs required for the photocatalytic mechanism. Investigations conducted by Nugroho revealed that $CoFe_2O_4/SiO_2/NiO$ composites with a band gap of 1.5 eV achieved methylene blue degradation efficiency of up to 99.30% under optimal conditions [56].

The underlying photocatalytic mechanism of methylene blue degradation involves the formation of reactive oxygen species (ROS) such as hydroxyl radicals (-OH) and superoxide anions ( $O_2^-$ ), which arise from electron-hole pairs generated through photon absorption [57]. With a band gap of 1.180 eV, the energy available for ROS formation is sufficient to efficiently oxidize the complex bonds present in the methylene blue structure. This energetic advantage also reduces the tendency for electron-hole recombination, a

major limiting factor in photocatalytic efficiency. The optimal positions of the conduction band and valence band energy levels facilitate efficient electron transfer, thereby generating the active species required for methylene blue degradation [58].

The derived band gap value of 1.180 eV is in remarkable agreement with the prevailing research trend regarding spinel ferrite materials used in photocatalytic efforts. Extensive investigations conducted by a research Holinsworth et al. that $CoFe_2O_4$ exhibits superior band gap properties when compared to its counterpart $NiFe_2O_4$, which exhibits an indirect band gap of 1.64 eV [54]. This disparity suggests that the incorporation of $Co^{2+}$ in the spinel framework results in a significant reduction in the band gap energy, directly enhancing the photocatalytic efficacy under visible light irradiation. This phenomenon can be explained by the stronger hybridization effect of $Co^{2+}$ *d* orbitals with $O^{2-}$ orbitals when compared to $Ni^{2+}$, leading to enhanced electron delocalization [59].

Comparative analysis with alternative ferrite materials further underlines the favorable position of $CoFe_2O_4$. Investigations on bismuth ferrite ($BiFeO_3$) revealed a band gap of 1.9 eV, indicating adept dye degradation ability [60], however this increased value reduces the visible light absorption efficiency relative to $CoFe_2O_4$. Simultaneously, the g-$C_3N_4$/$CoFe_2O_4$ composite exhibits an increased band gap compared to its individual constituents, indicating that the formation of heterostructures has the potential to alter the electronic properties of the material [61]. Nevertheless, for pure photocatalytic applications without the composite, the band gap of 1.180 eV of $CoFe_2O_4$ achieves an optimal balance between effective light absorption and sufficient energy for the activation of the photocatalytic mechanism.

### 3.5. EDX Characterization

The $CoFe_{1-2}$ compound exhibits an elemental composition consisting of 31.77% oxygen (O), 40.30% iron (Fe), 20.69% cobalt (Co), and 7.24% silicon (Si), forming a metal ratio of 2:1 (Table 3). The percentage quantification of these elements corroborates the formation of cobalt ferrite ($CoFe_2O_4$) structure, coupled with the inclusion of silica ($SiO_2$) as a supporting medium. The Fe:Co ratio is close to 2:1 (40.30%: 20.69%) in line with the ideal stoichiometric framework of spinel ferrite $CoFe_2O_4$, thus confirming the efficacy of the synthesis methodology. The detection of silicon at 7.24% suggests surface modification via silica or its integration into the material architecture, potentially enhancing the stability and dispersion of nanoparticles in the photocatalytic context.

The $CoNi_{1-1}$ material exhibits distinct compositional characteristics, with 88.54% cobalt (Co) and 11.46% nickel (Ni), resulting in a metal ratio of 8:1. The absence of oxygen percentage data in this specimen is noteworthy, as it may imply a structure largely influenced by metal-metal interactions or the presence of a CoNi alloy exhibiting more pronounced metallic properties. The increased Co:Ni ratio (8:1) suggests cobalt as the major constituent in this material, with nickel acting as a minor dopant capable of modulating the electronic and catalytic attributes of the composite.

This compositional investigation is in line with a previous study by Alshorifi et al., who presented EDX data on $CoFe_2O_4$ with a composition of Co (58.2%), Fe (23.3%), and O (18.5%), indicating the production of high-purity $CoFe_2O_4$ nanoparticles [62]. Despite the variation in elemental percentage figures, the analogous elemental distribution patterns support the successful synthesis of cobalt-ferrite-based materials in this study.

The 2:1 metal ratio in $CoFe_{1-2}$ indicates the development of an ideal spinel ferrite configuration represented by the formula $CoFe_2O_4$, where $Co^{2+}$ ions occupy tetrahedral sites while $Fe^{3+}$ ions reside in octahedral sites in the crystal framework. The presence of silicon (7.24%) suggests modifications involving silica that can develop a protective layer on the nanoparticle surface, enhance thermal and chemical stability, and reduce particle agglomeration. Such silica modification is consistent with the investigation by Dorri et al., who documented the synthesis of $CoFe_2O_4$/$SiO_2$ as an early stage in the evolution of composite photocatalytic materials [63]. In contrast, the composition of $CoNi_{1-1}$, with cobalt dominance (88.54%) and relatively small nickel content (11.46%), implies the formation of a cobalt-centric structure through nickel doping. The substantial Co:Ni ratio (8:1) suggests that nickel acts as a dopant capable of changing the electronic configuration of cobalt-based materials.

Table 3. Elemental composition analysis by EDX.

| Sample | (%wt) | | | | | Metal ratio |
|---|---|---|---|---|---|---|
| | O | Fe | Co | Ni | Si | |
| $CoFe_{1-2}$ | 31.77 | 40.30 | 20.69 | - | 7.24 | 2:1 |
| $CoNi_{1-1}$ | - | - | 88.54 | 11.46 | - | 8:1 |

These changes can lead to significant modifications in the optical, electrical, and catalytic characteristics of the compounds.

The elemental composition identified in $CoFe_{1-2}$ materials has substantial implications for their photocatalytic efficacy in methylene blue degradation. Research conducted by Saady & Ebahim showed that the $CoFe_2O_4$ based materials have a band gap of about 3.1 eV, which is conducive to photocatalytic activation under light irradiation [64]. Although this band gap value is relatively higher compared to certain other photocatalytic materials, the incorporation of silica (7.24% Si) can affect the surface properties and enhance the adsorption of methylene blue, a critical phase in the photocatalytic degradation process.

The optimum photocatalytic activity has been established for $CoFe_{1-2}$ at a metal ratio of 2:1 (Fe:Co), as evidenced by various investigations. The significant iron content (40.30%) significantly enhances the magnetic characteristics of the material, facilitating the direct separation and recycling of the catalyst after degradation. In contrast, cobalt (20.69%) plays a significant role in enhancing the visible light absorption and minimizing the band gap, thus enhancing the photocatalytic performance under solar irradiation.

The material categorized as $CoNi_{1-1}$, characterized by a metal ratio of 8:1 (Co:Ni), exhibits a very different composition and can provide various catalytic mechanisms. The dominance of cobalt (88.54%) along with nickel (11.46%) fosters a material with superior magnetic and catalytic attributes. Nickel has been shown to enhance the electrical conductivity and electron mobility in the photocatalytic mechanism, which can accelerate the formation of hydroxyl radicals essential for the degradation of methylene blue [65].

Previous investigations by Dorri *et al*. showed that the incorporation of silica into materials such as $CoFe_{1-2}$ can improve nanoparticle dispersion and reduce agglomeration, thereby increasing the active surface area available for pollutant adsorption and degradation [63]. The inclusion of silicon (7.24%) in $CoFe_{1-2}$ can also contribute to the enhancement of catalyst stability and durability during successive photocatalytic applications.

Given its elemental composition, $CoFe_{1-2}$ is anticipated to exhibit more balanced photocatalytic efficacy compared to $CoNi_{1-1}$ in methylene blue degradation. This statement is corroborated by a study conducted by Alshorifi *et al.* who compared the photocatalytic efficacy of ferrite-based materials, revealing that methylene blue degradation reached 96.89% with $ZnFe_2O_4$, while the $CoFe_2O_4$ based material showed commendable performance, although slightly lower [62].

The incorporation of silica in $CoFe_{1-2}$ has the potential to enhance the adsorption capacity of methylene blue on the catalyst surface, a critical initial phase in the photocatalytic process. Effective adsorption enhances the interaction between target molecules and photocatalytic active sites, thereby enhancing the degradation efficiency. Furthermore, a 2:1 ratio of Fe and Co has been shown to produce optimal magnetic properties and significant redox activity for the conversion of organic pollutants.

$CoNi_{1-1}$, with a metal ratio of 8:1, has the potential to exhibit enhanced magnetic properties due to the increased cobalt concentration, which is beneficial for magnetically assisted catalyst separation after the degradation process. However, the lack of oxide components or supporting frameworks such as silica may reduce the specific surface area and long-term stability of this catalyst under photocatalytic reaction conditions.

### 3.6. Photodegradation of Methylene Blue

In the early phase of the experiment, which took place in the dark for 20 minutes, both catalysts showed minimal degradation efficiency. The efficiency of the photocatalyst is calculate by the formula:

$$\%\, Efficiency = \frac{(C_0 - C_t)}{C_0} \times 100\% \qquad (1)$$

where $C_0$ means the initial concentration of the sample and $C_t$ is the concentration at the degradation time. The $CoFe_{1-2}$ catalyst was only able to achieve degradation of around 15% at 20 minutes, while $CoNi_{1-1}$ showed even lower performance with degradation only reaching around 5% (Figure 5). This phenomenon is in line with the findings of previous studies which

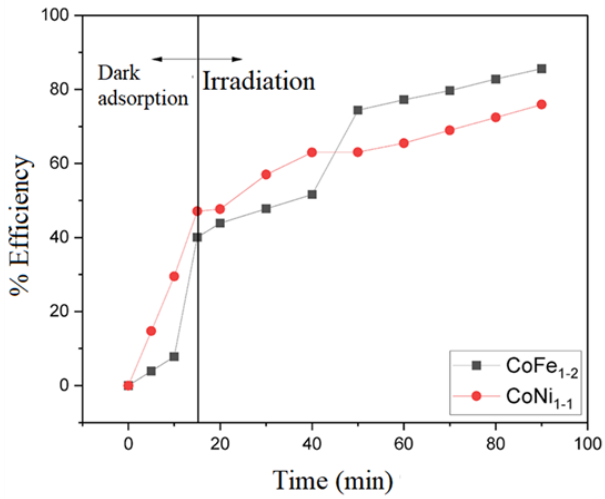


Figure 5. Effect of contact time on methylene blue's degradation efficiency.

showed that in dark conditions low degradation values were obtained because there was no light source so that the photon energy to produce -OH radicals was weak [66]. The low catalytic activity in dark conditions indicates that the degradation process of methylene blue is highly dependent on the photocatalytic mechanism rather than pure adsorption or dark catalytic reactions.

The difference in performance between the two catalysts in the dark can be attributed to the differences in the intrinsic properties of the materials. The iron-cobalt ($CoFe_{1-2}$) based catalyst showed slightly better activity compared to the nickel-cobalt ($CoNi_{1-1}$) catalyst, which is likely due to the differences in electronic band structure and surface properties that affect the interaction with methylene blue molecules even without light activation.

A significant transformation was observed after the illumination of the system at 20 min, where both catalytic materials showed a marked increase in degradation activity. The $CoFe_2O_4$ catalyst showed a more pronounced gradient compared to $CoNi_{1-1}$, indicating a superior degradation rate. In the initial 20-minute interval after exposure (20-40 minutes), $CoFe_2O_4$ successfully increased the degradation from 15% to about 62%, while $CoNi_{1-1}$ increased from 5% to about 47%. This significant spike in activity is in line with the photocatalytic mechanism, where the photon energy facilitates the excitation of electrons from the valence band to the conduction band, generating electron-hole pairs that are then involved in the degradation process.

BET analysis revealed that $CoFe_{1-2}$ has a higher specific surface area (104.526 m²/g) than $CoNi_{1-1}$ (83.160 m²/g), providing more active sites for adsorption and photocatalytic reactions. Although $CoNi_{1-1}$ has a larger pore diameter (9.97 nm vs. 3.61 nm), the superior surface area of $CoFe_{1-2}$ was more significant in determining the photocatalytic activity. UV-DRS characterization showed that $CoFe_{1-2}$ has a narrow band gap (1.180 eV), allowing efficient activation under visible light and utilization of a broader light spectrum. Others investigations showed that $CoFe_2O_4$ has an energy band gap of about 2.7 eV [64], thus enabling photocatalytic activation under visible light conditions. This activation generates reactive species such as hydroxyl radicals (-OH), superoxide radicals ($O_2^-$), and holes ($h^+$), which are integral to the degradation of organic compounds. The hierarchy of influence of these reactive species on the photocatalytic efficacy is documented as follows: $H_2O_2 > h^+ > e^- > O_2^- >$ -OH, explaining the apparent effectiveness of the photocatalytic mechanism in the degradation of methylene blue [64].

Longitudinal kinetic analysis revealed that both catalysts exhibited relatively uniform degradation trajectories post-light activation, albeit at different rates. $CoFe_2O_4$ reached a peak degradation of approximately 85% at the end of the experiment (90 min), while $CoNi_{1-1}$ reached approximately 75%. The variance in performance can be attributed to differences in crystal structure, particle dimensions, and magnetic characteristics of each material. $CoFe_2O_4$ based materials have been documented to have increased saturation magnetization, such as 39.9 emu/g for pure $CoFe_2O_4$ [64], facilitating post-reaction catalyst uptake and potentially affecting the distribution of active sites on the catalyst surface.

The underlying mechanism of methylene blue photodegradation over cobalt-iron and cobalt-nickel based catalysts involves a series of complex reactions starting from the activation of the photocatalyst leading to the complete mineralization of the dye molecules. This progression occurs through a phase of electronic activation on the catalyst surface, generation of reactive species, and a succession of oxidation reactions culminating in the formation of end products in the guise of simple inorganic entities such as $CO_2$, $H_2O$, and mineral ions.

The initial phase of the photodegradation mechanism begins with the absorption of a photon by the photocatalyst material when the energy of the absorbed photon is equal to or exceeds the band gap of the material. For $CoFe_2O_4$, the activation process can be represented as follows [35]:

$$CoFe_2O_4 + h\nu \rightarrow CoFe_2O_4\ (e^{-}_{cb} + h^{+}_{vb}) \quad (2)$$

In this equation, a photon with sufficient energy excites an electron from the valence band to the conduction band, generating a positively charged hole in the valence band. This electron-hole pair is an important species responsible for the photocatalytic efficacy of the material. However, these electron-hole pairs are also susceptible to recombination, which generates heat and reduces the photocatalytic efficiency, as represented by the reaction [67]:

$$e^{-}_{cb} + h^{+}_{vb} \rightarrow \text{heat} \quad (3)$$

The efficiency of the photocatalytic process largely depends on the material's capacity to reduce electron-hole recombination and optimize electron transfer to species adsorbed on the catalyst surface. $CoFe_2O_4$ material shows advantages in this aspect due to the spinel configuration of ferrite, which promotes a more favorable electron distribution between $Co^{2+}$ and $Fe^{3+}$ ions, thus reducing the recombination rate.

Electrons excited to the conduction band, together with holes in the valence band, actively

contribute to the formation of reactive species that facilitate the degradation of methylene blue. Electrons in the conduction band are involved in reactions with dissolved oxygen, producing superoxide radicals [67]:

$$e^{-cb} + O_2 \rightarrow -O_2^- \quad (4)$$

Furthermore, these superoxide radicals react with water to produce hydroxide ions and hydrogen peroxide:

$$\bullet O_2^- + H_2O \rightarrow OH^- + H_2O_2 \quad (5)$$

Simultaneously, holes present in the valence band interact with hydroxide ions or water molecules adsorbed on the catalyst surface, resulting in the formation of highly reactive hydroxyl radicals:

$$h^{+vb} + OH^- \rightarrow -OH \quad (6)$$
$$h^{+vb} + H_2O \rightarrow -OH + H^+ \quad (7)$$

Hydroxyl radicals (-OH) are known as strong oxidizing agents, having a redox potential of 2.8 V, allowing them to oxidize a wide range of organic compounds, including methylene blue. In addition, positive holes can also directly oxidize organic molecules adsorbed on the catalyst surface.

The photodegradation kinetics of methylene blue (MB) by both $CoFe_{1-2}$ and $CoNi_{1-1}$ samples were evaluated using pseudo-zero-order, pseudo-first-order, and pseudo-second-order kinetic models (Table 4). Among these, the pseudo-first-order model exhibited the best linear correlation with experimental data, as evidenced by the highest $R^2$ values of 0.9206 for $CoFe_{1-2}$ and 0.8832 for $CoNi_{1-1}$. These coefficients are significantly higher than those obtained for the pseudo-zero-order ($R^2$ = 0.8773 for $CoFe_{1-2}$; 0.7702 for $CoNi_{1-1}$) and pseudo-second-order models ($R^2$ = 0.2216 for $CoFe_{1-2}$; 0.1531 for $CoNi_{1-1}$), indicating a superior fit. This suggests that the rate of MB photodegradation is more accurately described by a mechanism where the degradation rate is directly proportional to the concentration of the dye, consistent with a first-order reaction pathway [68].

The pseudo-zero-order model can be expressed as:

$$C_0 - C_t = kt \quad (8)$$

The pseudo-first-order model can be expressed as:

$$ln\left(\frac{C_0}{C_t}\right) = -kt \quad (10)$$

The pseudo-second-order model can be expressed as:

$$\frac{1}{C_t} - \frac{1}{C_0} = kt \quad (11)$$

The kinetic rate constants ($k_1$) obtained from the pseudo-first-order model 0.0093 $min^{-1}$ for $CoFe_{1-2}$ and 0.0080 $min^{-1}$ for $CoNi_{1-1}$ further support this conclusion by reflecting a consistent and moderate degradation rate over time. The relatively poor correlation coefficients in the zero- and second-order models imply that neither a constant degradation rate (as assumed in the zero-order model) nor a bimolecular reaction mechanism (as assumed in the second-order model) adequately describes the degradation kinetics under the applied conditions. Therefore, the pseudo-first-order model is more appropriate for representing the photodegradation behavior of methylene blue using these mesostructured photocatalysts, reinforcing the predominance of surface-mediated first-order reaction kinetics governed by the availability of active sites and MB adsorption dynamics.

The superior fit of the pseudo-first-order kinetic model for both $CoFe_{1-2}$ and $CoNi_{1-1}$ in describing methylene blue (MB) photodegradation is further substantiated by the adsorption behavior and surface properties of the catalysts. The higher experimentally determined adsorption capacity ($Exp.\ q_e$) of $CoFe_{1-2}$ (171.184 mg/g) compared to $CoNi_{1-1}$ (151.841 mg/g) reflects a greater availability of active sites and potentially higher surface area, which enhances MB uptake and facilitates surface-mediated photocatalytic reactions. These characteristics align with prior

Table 4. Kinetic parameters of $CoFe_{1-2}$ and $CoNi_{1-1}$ based on pseudo first and second order models.

| Sampel | Pseudo zero orde model | | Pseudo first orde model | | Pseudo second orde model | |
|---|---|---|---|---|---|---|
| | $k_1$ | $R^2$ | $k_1$ | $R^2$ | $k_2$ | $R^2$ |
| $CoFe_{1-2}$ | 10.029 | 0.8773 | 0.0093 | 0.9206 | 3.3152 | 0.2216 |
| $CoNi_{1-1}$ | 20.407 | 0.7702 | 0.0080 | 0.8832 | 2.1316 | 0.1531 |

findings on $CoFe_2O_4$-based materials, whose spinel structures are known to offer abundant and stable adsorption sites for organic dyes. The pseudo-first-order model not only yields the best correlation coefficients ($R^2 = 0.9206$ for $CoFe_{1\text{-}2}$ and 0.8832 for $CoNi_{1\text{-}1}$) but also provides calculated adsorption capacities ($Cal.\ q_e$) that closely approximate experimental values, particularly for $CoNi_{1\text{-}1}$. For the $CoFe_{1\text{-}2}$, the slightly overestimated $Cal.\ q_e$ (249.6319 mg/g) may suggest a more complex adsorption-desorption dynamic or heterogeneous distribution of active sites, reinforcing the model's sensitivity to material-specific surface characteristics.

Although the rate constants ($k_1$) derived from the pseudo-first-order model were negative for both samples (–0.00938 $min^{-1}$ for $CoFe_{1\text{-}2}$ and –0.00803 $min^{-1}$ for $CoNi_{1\text{-}1}$), which is atypical, such deviations have been reported in systems where desorption or surface restructuring effects compete with adsorption processes [69]. This anomaly may also be attributed to limitations in data fitting or experimental inconsistencies during time-resolved measurements. Nonetheless, the high conformity of kinetic modeling to the pseudo-first-order mechanism, supported by congruent adsorption capacity data and superior surface performance of $CoFe_{1\text{-}2}$, suggests that the dominant photodegradation mechanism proceeds via physisorption-controlled kinetics, particularly governed by the initial concentration of MB at the catalyst surface [70]. These findings not only validate the appropriateness of the pseudo-first-order kinetic model but also emphasize the significance of material-specific surface properties in dictating adsorption-driven photodegradation efficiency.

## 4. Conclusions

This study confirms that controlled cobalt–iron and cobalt–nickel ratios are key drivers of photocatalytic efficiency. Using a template-assisted synthesis with mesoporous silica–gelatin (SPG-20), $CoFe_{1\text{-}2}$ and $CoNi_{1\text{-}1}$ nanostructures were obtained with distinct physicochemical properties. $CoFe_{1\text{-}2}$ exhibited a higher surface area (104.526 $m^2/g$), narrower band gap (1.180 eV), and greater adsorption capacity (171.184 mg/g) compared to $CoNi_{1\text{-}1}$ (83.160 $m^2/g$; band gap 1.856 eV), leading to superior methylene blue degradation (85% vs. 75% within 90 min). These results advance current knowledge by demonstrating that a 2:1 Fe:Co ratio optimizes structural and electronic features, enabling more efficient visible-light-driven photocatalysis and offering a promising strategy for sustainable treatment of textile wastewater.

## Acknowledgments

The authors gratefully acknowledge the financial support provided by Universitas Sebelas Maret through the Riset Penelitian Unggulan Terapan (PUTA) Scheme under grant number 369/UN27.22/PT.01.03/2025. This support was instrumental in facilitating the research, analysis, and completion of this study.

## CRedit Author Statement

Author Contributions: M. Ulfa: Conceptualization, Investigation, Methodology, Formal Analysis, Resources, Data Curation, Writing – Original Draft, Writing – Review & Editing, Supervision, Project Administration; I.S. Rohmah: Validation, Writing – Review & Editing, Data Curation; C.N. Anggreani: Methodology, Formal Analysis, Data Curation, Writing – Original Draft Preparation. All authors have read and agreed to the published version of the manuscript.

## References

[1] Dutta, S., Adhikary, S., Bhattacharya, S., Roy, D., Chatterjee, S., Chakraborty, A., Banerjee, D., Ganguly, A., Nanda, S., Rajak, P. (2024). Contamination of textile dyes in aquatic environment: Adverse impacts on aquatic ecosystem and human health, and its management using bioremediation. *Journal of Environmental Management*, 353(October 2023), 120103. DOI: 10.1016/j.jenvman.2024.120103.

[2] Periyasamy, A.P. (2024). Recent Advances in the Remediation of Textile-Dye-Containing Wastewater: Prioritizing Human Health and Sustainable Wastewater Treatment. Sustainability (Switzerland), 16(2). DOI: 10.3390/su16020495.

[3] Islam, M., Rakha, A., Nawaj, J., Mondal, H. (2025). A critical review on textile dye-containing wastewater : Ecotoxicity , health risks , and remediation strategies for environmental safety. *Cleaner Chemical Engineering*, 11(January), 100165. DOI: 10.1016/j.clce.2025.100165.

[4] Oladoye, P.O., Ajiboye, T.O., Omotola, E.O., Oyewola, O.J. (2022). Methylene blue dye: Toxicity and potential elimination technology from wastewater. *Results in Engineering*, 16, 100678. DOI: 10.1016/j.rineng.2022.100678.

[5] Ahmadi, S., Igwegbe, C.A. (2020). Removal of Methylene Blue on Zinc Oxide Nanoparticles: Nonlinear and Linear Adsorption Isotherms and Kinetics Study. *Sigma Journal of Engineering and Natural Sciences*, 38(1), 289–303.

[6] Nabilah, B., Purnomo, A.S., Prasetyoko, D., Rohmah, A.A. (2023). Methylene Blue biodecolorization and biodegradation by immobilized mixed cultures of Trichoderma viride and Ralstonia pickettii into SA-PVA-Bentonite matrix. *Arabian Journal of Chemistry*, 16(8), 104940. DOI: 10.1016/j.arabjc.2023.104940.

[7] Hu, Y., Wang, H., Ren, X., Wu, F., Liu, G., Zhang, S., Luo, H., Fang, L. (2024). Enhancing Methylene Blue Adsorption Performance of Ti3C2Tx@Sodium Alginate Foam Through Pore Structure Regulation. *Nanomaterials*, 14(23) DOI: 10.3390/nano14231925.

[8] Swaminaathan, P., Saravanan, A., Yaashikaa, P.R., Vickram, A.S. (2024). Recent advances in photocatalytic degradation of persistent organic pollutants: Mechanisms, challenges, and modification strategies. *Sustainable Chemistry for the Environment*, 8(September), 100171. DOI: 10.1016/j.scenv.2024.100171.

[9] Balu, S., Ganapathy, D., Arya, S., Atchudan, R., Sundramoorthy, A.K. (2024). Advanced photocatalytic materials based degradation of micropollutants and their use in hydrogen production - a review. *RSC Advances*, 14(20), 14392–14424. DOI: 10.1039/d4ra01307g.

[10] Rahman, M., Shaheen, S., Ahmad, T. (2025). Photocatalytic transformation of organic pollutants and remediation strategies of carbon emissions and nitrogen fixation in inland water. *Materials Today Catalysis*, 9(April), 100103. DOI: 10.1016/j.mtcata.2025.100103.

[11] Chen, K., Qu, F., Huang, Y., Cai, J., Wu, F., Li, W. (2024). Advancing photocatalytic concrete technologies in design, performance and application for a sustainable future. *Advanced Nanocomposites*, 1(1), 180–200. DOI: 10.1016/j.adna.2024.05.002.

[12] Iyyappan, J., Gaddala, B., Gnanasekaran, R., Gopinath, M., Yuvaraj, D., Kumar, V. (2024). Critical review on wastewater treatment using photo catalytic advanced oxidation process: Role of photocatalytic materials, reactor design and kinetics. *Case Studies in Chemical and Environmental Engineering*, 9(December 2023), 100599. DOI: 10.1016/j.cscee.2023.100599.

[13] Yang, T., Zhang, H., Pang, B., Wong, J.W.C. (2025). Recent Advances in Transition Metal-Based Metal-Organic Frameworks for Hydrogen Production. *Small Science*, 2400446. DOI: 10.1002/smsc.202400446.

[14] Li, X.P., Huang, C., Han, W.K., Ouyang, T., Liu, Z.Q. (2021). Transition metal-based electrocatalysts for overall water splitting. *Chinese Chemical Letters*, 32(9), 2597–2616. DOI: 10.1016/j.cclet.2021.01.047.

[15] Guo, S., Zheng, L., Wang, X., Yang, H., Wang, T., Li, L., Zhang, Y., Zhao, G., Li, T. (2024). Trace Iron-Doped Nickel-Cobalt selenide with rich heterointerfaces for efficient overall water splitting at high current densities. *Journal of Colloid and Interface Science*, 674(April), 902–912. DOI: 10.1016/j.jcis.2024.06.226.

[16] Gatou, M.A., Syrrakou, A., Lagopati, N., Pavlatou, E.A. (2024). Photocatalytic TiO2-Based Nanostructures as a Promising Material for Diverse Environmental Applications: A Review. *Reactions*, 5(1), 135–194. DOI: 10.3390/reactions5010007.

[17] Rizqi Maulana, M.A., Aisyaturridha, Salmah Cholilah, Dwi Arista, F., Bagus Nur Listiyono (2023). Nickel Oxide (NiO) Thin Film Synthesis via Electrodeposition for Methylene Blue Photodegradation. *Chemistry and Materials*, 2(3), 61–66. DOI: 10.56425/cma.v2i3.62.

[18] Revathi, J., Abel, M.J., Archana, V., Sumithra, T., Thiruneelakandan, R., Joseph prince, J. (2020). Synthesis and characterization of CoFe2O4 and Ni-doped CoFe2O4 nanoparticles by chemical Co-precipitation technique for photo-degradation of organic dyestuffs under direct sunlight. *Physica B: Condensed Matter*, 587, 412136. DOI: 10.1016/j.physb.2020.412136.

[19] Kalam, A., Al-Sehemi, A.G., Assiri, M., Du, G., Ahmad, T., Ahmad, I., Pannipara, M. (2018). Modified solvothermal synthesis of cobalt ferrite (CoFe2O4) magnetic nanoparticles photocatalysts for degradation of methylene blue with H2O2/visible light. *Results in Physics*, 8, 1046–1053. DOI: 10.1016/j.rinp.2018.01.045.

[20] Kibona, T.E. (2020). Synthesis of NiCo2O4/mesoporous carbon composites for supercapacitor electrodes. *Journal of Solid State Electrochemistry*, 24(7), 1587–1598. DOI: 10.1007/s10008-020-04673-4.

[21] Safdar, A., Mohamed, H.E.A., Muhaymin, A., Hkiri, K., Matinise, N., Maaza, M. (2024). Biogenic synthesis of nickel cobaltite nanoparticles via a green route for enhancing the photocatalytic and electrochemical performances. *Scientific Reports*, 14(1), 1–17. DOI: 10.1038/s41598-024-68574-6.

[22] Jayan, G., Elias, L., Anil, A., Bhagya, T.C., Shibli, S.M.A. (2024). Step-by-step tuning of morphology and band gap of ZnS/MoS2 photocatalyst for enhanced visible light to hydrogen fuel conversion. *International Journal of Hydrogen Energy*, 51(PC), 1375–1386. DOI: 10.1016/j.ijhydene.2023.11.102.

[23] Ansari, A.S., Azzahra, G., Nugroho, F.G., Mujtaba, M.M., Ahmed, A.T.A. (2025). Oxides and Metal Oxide/Carbon Hybrid Materials for Efficient Photocatalytic Organic Pollutant Removal. *Catalysts*, 15(2), 1–43. DOI: 10.3390/catal15020134.

[24] Kamakshi, T., Sundari, G.S. (2020) Photocatalytic Degradation of Methylene Blue via Cobalt Doped Fe3O4 Nanoparticles. *Asian J. Chem.*, 32, 1413–1420. DOI: 10.14233/ajchem.2020.22621

[25] Chen, L., Ren, X., Alharbi, N.S., Chen, C. (2021). Fabrication of a novel Co/Ni-MOFs@BiOI composite with boosting photocatalytic degradation of methylene blue under visible light. *Journal of Environmental Chemical Engineering*, 9(5), 106194. DOI: 10.1016/j.jece.2021.106194.

[26] Istiqomah, N.I., Larasati, D.A., Hanifah, A.N.A., Olivia, L., Oshima, D., Kato, T., Suharyadi, E. (2023). Photocatalytic Removal of Methylene Blue Dye Using CoZnFe2O4/SiO2 Magnetic Nanoparticles. *Key Engineering Materials*, 940, 55–64. DOI: 10.4028/p-o402y2.

[27] Lenni, N., Lubis, R.Y., Masthura. (2025). Material Nanopartikel Fotokatalis Fe3o4/Sio2/Tio2 Untuk Degradasi Methylene Blue. *Jurnal Rekayasa Material, Manufaktur dan Energi*, 8(1), 59–65. DOI: 10.30596/rmme.v8i1.21752.

[28] Vasiljevic, Z.Z., Dojcinovic, M.P., Vujancevic, J.D., Jankovic-Castvan, I., Ognjanovic, M., Tadic, N.B., Stojadinovic, S., Brankovic, G.O., Nikolic, M. V. (2020). Photocatalytic degradation of methylene blue under natural sunlight using iron titanate nanoparticles prepared by a modified sol-gel method: Methylene blue degradation with Fe2TiO5. *Royal Society Open Science*, 7(9). DOI: 10.1098/rsos.200708.

[29] Murugesan, A., Loganathan, M., Senthil Kumar, P., Vo, D.V.N. (2021). Cobalt and nickel oxides supported activated carbon as an effective photocatalysts for the degradation Methylene Blue dye from aquatic environment. *Sustainable Chemistry and Pharmacy*, 21(December 2020), 100406. DOI: 10.1016/j.scp.2021.100406.

[30] Puspitasari, P., Budi, L.S. (2020). Physical and magnetic properties comparison of cobalt ferrite nanopowder using sol-gel and sonochemical methods. *International Journal of Engineering, Transactions B: Applications*, 33(5), 877–884. DOI: 10.5829/IJE.2020.33.05B.20.

[31] Khan, I., Saeed, K., Khan, I. (2019). Nanoparticles: Properties, applications and toxicities. *Arabian Journal of Chemistry*, 12(7), 908–931. DOI: 10.1016/j.arabjc.2017.05.011.

[32] Setiadi, E.A., Shabrina, N., Budi Utami, H.R., Fahmi, N.F., Kato, T., Iwata, S., Suharyadi, E. (2016). Sintesis Nanopartikel Cobalt Ferrite (CoFe2O4) dengan Metode Kopresipitasi dan Karakterisasi Sifat Kemagnetannya. *Indonesian Journal of Applied Physics*, 3(01), 55. DOI: 10.13057/ijap.v3i01.1216.

[33] Cai, Z., Park, J., Park, S. (2023). Synthesis of Flower-like ZnO and Its Enhanced Sensitivity towards NO2 Gas Detection at Room Temperature. *Chemosensors*, 11(6). DOI: 10.3390/chemosensors11060322.

[34] Jdidi, A.R., Nouira, W., Selmi, A., Drissi, N., Aissa, M., Hcini, S., Gassoumi, M. (2025). Impact of Calcination Temperature on the Properties and Photocatalytic Efficiency of Cd0.6Mg0.2Cu0.2Fe2O4 Spinel Ferrites Synthesized via the Sol–Gel Method. *Crystals*, 15(5). DOI: 10.3390/cryst15050457.

[35] Suaib, S., Aritonang, H., Koleangan, H.S.J. (2020). Sintesis Nanopartikel Cobalt Ferrite (CoFe2O4) Dengan Metode Kopresipitasi dan Aplikasinya Sebagai Fotokatalis. *Chemistry Progress*, 12(1), 49–53. DOI: 10.35799/cp.12.1.2019.27922.

[36] Zuliantoni, Z., Suprapto, W., Setyarini, P.H., Gapsari, F. (2022). Extraction and characterization of snail shell waste hydroxyapatite. *Results in Engineering*, 14(February), 100390. DOI: 10.1016/j.rineng.2022.100390.

[37] Tang, H., Wang, W., Zhou, J., Li, T., Shu, Z. (2022). Optimizing the Crystallinity of Heptazine-Based Crystalline Carbon Nitride by Regulating Temperature for Enhanced Photocatalytic H2 Evolution. *Journal of Nanomaterials*, 4923588. DOI: 10.1155/2022/4923588.

[38] Zhang, Y., Tang, Z.-R., Fu, X., Xu, Y.-J. (2010). TiO2−Graphene Nanocomposites for Gas-Phase Photocatalytic Degradation of Volatile Aromatic Pollutant: Is TiO2−Graphene Truly Different from Other TiO2−Carbon Composite Materials?. *ACS Nano*, 4(12), 7303–7314. DOI: 10.1021/nn1024219

[39] Wang, Y., Wang, X., Antonietti, M. (2012). Polymeric graphitic carbon nitride as a heterogeneous organocatalyst: From photochemistry to multipurpose catalysis to sustainable chemistry. *Angewandte Chemie - International Edition*, 51(1), 68–89. DOI: 10.1002/anie.201101182.

[40] Tripathy, S.R., Baral, S.S. (2025). Defect Engineering in Semiconductor Photocatalysts: Enhancing Photocatalytic Activity for Green Energy Production. *Advanced Energy and Sustainability Research*, 2500110. DOI: 10.1002/aesr.202500110.

[41] Guo, L., Gao, J., Huang, Q., Wang, X., Li, Z., Li, M., Zhou, W. (2024). Element engineering in graphitic carbon nitride photocatalysts. *Renewable and Sustainable Energy Reviews*, 199. DOI: 10.1016/j.rser.2024.114482.

[42] Thirumoolan, D., Ragupathy, S., Renukadevi, S., Rajkumar, P., Rai, R.S., Saravana Kumar, R.M., Hasan, I., Durai, M., Ahn, Y.H. (2024). Influence of nickel doping and cotton stalk activated carbon loading on structural, optical, and photocatalytic properties of zinc oxide nanoparticles. *Journal of Photochemistry and Photobiology A: Chemistry*, 448, 115300. DOI: 10.1016/j.jphotochem.2023.115300.

[43] Nandiyanto, A.B.D., Oktiani, R., Ragadhita, R. (2019). How to read and interpret ftir spectroscope of organic material. *Indonesian Journal of Science and Technology*, 4(1), 97–118. DOI: 10.17509/ijost.v4i1.15806.

[44] Almutairi, T.S. (2024). Unveiling the Impact of Spin and Cation Dynamics on Raman Spectroscopy in Co-Ferrite. *ACS Physical Chemistry Au*. 5, 2, 171–182. DOI: 10.1021/acsphyschemau.4c00088

[45] El-Masry, M.M., Arman, M.M. (2025). Cobalt, nickel and zinc spinel ferrites with high transmittance and UV-blocking for advanced optical applications. *Scientific Reports*, 15(1), 1–17. DOI: 10.1038/s41598-025-99604-6.

[46] Sivakumar, P., Ramesh, R., Ramanand, A., Ponnusamy, S., Muthamizhchelvan, C. (2011). Synthesis and characterization of nickel ferrite magnetic nanoparticles. *Materials Research Bulletin*, 46(12), 2208–2211. DOI: 10.1016/j.materresbull.2011.09.009.

[47] Palade, P., Comanescu, C., Kuncser, A., Berger, D., Matei, C., Iacob, N., Kuncser, V. (2020). Mesoporous cobalt ferrite nanosystems obtained by surfactant-assisted hydrothermal method: Tuning morpho-structural and magnetic properties via pH-variation. *Nanomaterials*, 10(3), 1–18. DOI: 10.3390/nano10030476.

[48] Chen, P.-K., Lai, N.-C., Ho, C.-H., Hu, Y.-W., Lee, J.-F., Yang, C.-M. (2013). New Synthesis of MCM-48 Nanospheres and Facile Replication to Mesoporous Platinum Nanospheres as Highly Active Electrocatalysts for the Oxygen Reduction Reaction. *Chemistry of Materials*, 25 (21), 4269–4277. DOI: 10.1021/cm402349f.

[49] Raja, P.M. V, Barron, A.R. (1934). Physical methods in chemistry. *Nature*, 134(3384), 366–367. DOI: 10.1002/jctb.5000533702.

[50] Baldovino-Medrano, V.G., Niño-Celis, V., Giraldo, R.I. (2023). Systematic Analysis of the Nitrogen Adsorption–Desorption Isotherms Recorded for a Series of Materials Based on Microporous–Mesoporous Amorphous Aluminosilicates Using Classical Methods. *Journal of Chemical & Engineering Data*, 68(9), 2512–2528. DOI: 10.1021/acs.jced.3c00257.

[51] Irwansyah, F.S., Amal, A.I., Diyanthi, E.W., Hadisantoso, E.P., Noviyanti, A.R., Eddy, D.R., Risdiana, R. (2024). How to Read and Determine the Specific Surface Area of Inorganic Materials using the Brunauer-Emmett-Teller (BET) Method. *ASEAN Journal of Science and Engineering*, 4(1), 61–70. DOI: 10.17509/ajse.v4i1.60748.

[52] Munawaroh, F., Masdya, Y., Baqiya, M.A., Triwikantoro, T. (2024). Indonesian Physical Review. *Indonesian Physical Review*, 7(2), 250–258. DOI: 10.29303/ip r.v7i2.313.

[53] Sing, K.S.W., Williams, R.T. (2004). Physisorption hysteresis loops and the characterization of nanoporous materials. *Adsorption Science and Technology*, 22(10), 773–782. DOI: 10.1260/0263617053499032.

[54] Holinsworth, B.S., Mazumdar, D., Sims, H., Sun, Q.C., Yurtisigi, M.K., Sarker, S.K., Gupta, A., Butler, W.H., Musfeldt, J.L. (2013). Chemical tuning of the optical band gap in spinel ferrites: CoFe 2O4 vs NiFe2O4. *Applied Physics Letters*, 103(8), 2011–2015. DOI: 10.1063/1.4818315.

[55] Choppin, G.R., Liljenzin, J.-O., Rydberg, J. (1995). Radiation Effects on Matter. *Radiochemistry and Nuclear Chemistry*, 166–191. DOI: 10.1016/b978-0-7506-2300-1.50011-7.

[56] Lenni, N., Lubis, R.Y., Masthura. (2025). Material Nanopartikel Fotokatalis Fe3o4/Sio2/Tio2 Untuk Degradasi Methylene Blue. *Jurnal Rekayasa Material, Manufaktur dan Energi*, 8(1), 59–65. DOI: 10.30596/rmme.v8i1.21752.

[57] Banerjee, S., Pillai, S.C., Falaras, P., O'shea, K.E., Byrne, J.A., Dionysiou, D.D. (2014). New insights into the mechanism of visible light photocatalysis. *Journal of Physical Chemistry Letters*, 5(15), 2543–2554. DOI: 10.1021/jz501030x.

[58] Barakat, N.A.M., Tolba, G.M.K., Khalil, K.A. (2022). Methylene Blue Dye as Photosensitizer for Scavenger-Less Water Photo Splitting: New Insight in Green Hydrogen Technology. *Polymers*, 14(3), 1–15. DOI: 10.3390/polym14030523.

[59] Song, M., Hou, L., Zhang, J., Zhang, J., Qian, G. (2025). A deeper orbital hybridization because of more unpaired electrons in d orbital resulted in a better catalytic performance. *Separation and Purification Technology*, 353(PC), 128639. DOI: 10.1016/j.seppur.2024.128639.

[60] Kalikeri, S., Shetty Kodialbail, V. (2021). Auto-combustion synthesis of narrow band-gap bismuth ferrite nanoparticles for solar photocatalysis to remediate azo dye containing water. *Environmental Science and Pollution Research*, 28(10), 12144–12152. DOI: 10.1007/s11356-020-10879-w.

[61] Weldekirstos, H.D., Mengist, T., Belachew, N., Mekonnen, M.L. (2024). Enhanced Photocatalytic Degradation of Methylene Blue Dye Using Fascily Synthesized G-C3N4/CoFe2O4 Composite under Sun Light Irradiation. *Results in Chemistry*, 7, 101306. DOI: 10.1016/j.rechem.2024.101306.

[62] Alkhobrani, S.H., Bayahia, H., Alshorifi, F.T. (2023). A Facile Synthesis of Metallic (Zn and Co) Ferrite Nanostructures as Efficient Solid Photocatalysts for Degradation of Methyl Orange and Methylene Blue under Sunlight. Iranian *Journal of Materials Science and Engineering*, 20(3), 1–12. DOI: 10.22068/ijmse.3284.

[63] Dorri, H., Zeraatkar Moghaddam, A., Ghiamati, E., Barikbin, B. (2022). A comprehensive study on the adsorption-photocatalytic processes using CoFe2O4/SiO2/MnO2 magnetic nanocomposite as a novel photo-catalyst for removal of Cr (VI) under simulated sunlight: Isotherm, kinetic and thermodynamic studies. *Journal of Environmental Health Science and Engineering*, 20(1), 147–165. DOI: 10.1007/s40201-021-00763-1.

[64] Al Saady, S.H., Ebrahim, S.E. (2024). Efficient Photocatalytic Degradation of Methylene Blue Using Magnetic CoFe2O4@CuO@Ag3VO4 Nanocomposite. *International Journal of Design and Nature and Ecodynamics*, 19(6), 1837–1846. DOI: 10.18280/ijdne.190601.

[65] Agboola, P.O., Shakir, I., Haider, S. (2022). Development of internal electric field induced NiFe2O4/CdO p-n nano-heterojunctions for solar light activated photodegradation of methylene blue dye. *Ceramics International*, 48(10), 13572–13579. DOI: 10.1016/j.ceramint.2022.01.236.

[66] Ahmad, I., Aslam, M., Jabeen, U., Zafar, M.N., Malghani, M.N.K., Alwadai, N., Alshammari, F.H., Almuslem, A.S., Ullah, Z. (2022). ZnO and Ni-doped ZnO photocatalysts: Synthesis, characterization and improved visible light driven photocatalytic degradation of methylene blue. *Inorganica Chimica Acta*, 543(July), 121167. DOI: 10.1016/j.ica.2022.121167.

[67] Priatmoko, S., Wahyuni, S. (2021). Fotokatalis Ni-N-TiO2 untuk Degradasi Metilen Biru. *Inovasi Sains dan Kesehatan*, 5, 120–165. DOI: 10.15294/.v0i0.17.

[68] Aurich, A., Hofmann, J., Oltrogge, R., Wecks, M., Gläser, R., Blömer, L., Mauersberger, S., Müller, R.A., Sicker, D., Giannis, A. (2017). Improved Isolation of Microbiologically Produced (2R,3S)-Isocitric Acid by Adsorption on Activated Carbon and Recovery with Methanol. *Organic Process Research and Development*, 21(6), 866–870. DOI: 10.1021/acs.oprd.7b00090.

[69] Huang, L., Zhang, L., Li, D., Xin, Q., Jiao, R., Hou, X., Zhang, Y., Li, H. (2020). Enhanced phenol degradation at near neutral pH achieved by core-shell hierarchical 4A zeolite/Fe@Cu catalyst. *Journal of Environmental Chemical Engineering*, 8(5), 103933. DOI: 10.1016/j.jece.2020.103933.

[70] Foo, K.Y., Hameed, B.H. (2010). Insights into the modeling of adsorption isotherm systems. *Chemical Engineering Journal*, 156(1), 2–10. DOI: 10.1016/j.cej.2009.09.013.